nature photonics | SUPPLEMENTARY INFORMATION
DOI: 10.1038/NPHOTON.2014.249

Network of time-multiplexed optical parametric oscillators as a coherent Ising machine

Alireza Marandi[1,2], Zhe Wang[1], Kenta Takata[2,3],
Robert L. Byer[1], and Yoshihisa Yamamoto[1,2,3]

[1] E. L. Ginzton Laboratory, Stanford University, California 94305, USA,

[2] National Institute of Informatics, Tokyo 101-8403, Japan,

[3] Department of Information and Communication Engineering, University of Tokyo,
Tokyo 113-8656, Japan.

1 Principle of Operation

The cartoon of Fig. 1c illustrates a comparison of search mechanisms of the OPO network and classical and quantum annealing. Classical simulated annealing employs a downward vertical search, in which the temperature is repeatedly decreased and increased until the ground state is found. Quantum annealing exerts a horizontal search in the energy landscape with quantum tunnelling. Therefore, with these methods, the computational time of finding the ground state increases with the increase in the number of metastable excited states or local minima. In contrast, the OPO-based Ising machine searches for the ground state in an upward direction. The total energy, i.e. the ordinate in Fig.1c, is now replaced by the network loss. The ground state (optimum solution) has a minimum loss as shown in the figure. If we put a parametric gain (G) into such a network and increase it gradually, the first touch to the network loss happens at the ground state (L_{min}), which results in the single-mode oscillation of the ground state spin configuration. At the pump rate above this threshold point, the parametric gain is clamped at the same value of $G = L_{min}$ due to nonlinear gain saturation, so that all the other modes including local minima stay under the oscillation threshold. If we use the terminology of "negative temperature" to represent the parametric gain, the mentioned upward search corresponds to the heating process from $T = -\infty$ for zero gain toward $T = -0$ for high gain. In this sense, the OPO machine is a "heating machine" while the classical simulated annealing is a "cooling machine."

2 Theoretical Modelling and Numerical Test of OPO Network

Femtosecond OPOs can be modelled by multimode analysis in the frequency domain as presented in [31]. Here for numerical simplicity, to simulate a network of N degenerate OPOs, we start with the quantum mechanical Fokker-Planck equation (Q-FPE) for a single continuous wave OPO using the generalised P-representation [32]:

$$\frac{d}{dt}P(a_s,b_s)=\left\{\frac{\partial}{\partial a_s}[a_s-(p-a_s^2)b_s)]+\frac{\partial}{\partial b_s}[b_s-(p-b_s^2)a_s)]\right\}P(a_s,b_s)$$
$$+\frac{1}{2A_s^2}\left[\frac{\partial^2}{\partial a_s^2}(p-a_s^2)+\frac{\partial^2}{\partial b_s^2}(p-b_s^2)\right]P(a_s,b_s). \quad \text{(S-1)}$$

Here $a_s=\alpha_s/A_s$ and $b_s=\beta_s/A_s$ are the normalised eigenvalues for the off-diagonal coherent-state expansion, $|\alpha_s\rangle\langle\beta_s|$, of the density matrix, γ_s and γ_p are the signal and pump photon decay rates, $A_s=(\gamma_p\gamma_s/2\kappa^2)^{1/2}$ is the oscillation field amplitude at a normalised pump rate $p=F_p/F_{th}=2$, $t=\frac{\gamma_s}{2}\tau$ is the normalised time, F_p is the pump field amplitude, $F_{th}=\gamma_s\gamma_p/4\kappa$ is the threshold pump amplitude. The average amplitudes of in-phase and quadrature-phase components of the signal wave are obtained by

$$\langle A_{s1}\rangle=A_s\langle a_s+b_s\rangle/2,$$
$$\langle A_{s2}\rangle=A_s\langle a_s-b_s\rangle/2i. \quad \text{(S-2)}$$

Equation S-1 can be cast into the c-number Langevin equation (C-LGE) for the in-phase and quadrature-phase components of the signal field via the Kramers-Moyal expansion [33]:

$$\frac{d}{dt}c=(-1+p-c^2-s^2)c+f^c$$
$$\frac{d}{dt}s=(-1-p-c^2-s^2)s+f^s. \quad \text{(S-3)}$$

where $c=\frac{1}{2}(a_s+b_s)$ and $s=\frac{1}{2i}(a_s-b_s)$, and f^c and f^s correspond to in-phase and quadrature-phase components of quantum noise of the OPO, which include both the incident vacuum fluctuations at signal frequency ω_s and pump frequency ω_p.

The equivalence of the Q-FPE (S-1) and the C-LGE (S-3) can be confirmed by comparing the squeezing and anti-squeezing characteristics of the two quadrature components using

$$\langle\Delta A_{s1}^2\rangle=A_s^2\langle(a_s+b_s)^2\rangle+1/4-\langle A_{s1}\rangle^2,$$
$$\langle\Delta A_{s2}^2\rangle=-A_s^2\langle(a_s-b_s)^2\rangle+1/4-\langle A_{s2}\rangle^2, \quad \text{(S-4)}$$

for the Q-FPE and

$$\langle\Delta A_{s1}^2\rangle=A_s^2(\langle c^2\rangle-\langle c\rangle^2),$$
$$\langle\Delta A_{s2}^2\rangle=A_s^2(\langle s^2\rangle-\langle s\rangle^2), \quad \text{(S-5)}$$

for the C-LGE. As shown in Fig. 1 in [7], the degrees of squeezing and anti-squeezing obtained by the two methods completely agree at pump rates around the threshold ($p=1$).

The Q-FPE and C-LGE for an injection-locked laser oscillator [34] can be extended to the mutually coupled degenerate OPOs using equation S-1 or S-3. The resulting C-LGEs for a network of degenerate OPOs are given by

$$\frac{d}{dt}c_j=\left\{[-1+p-(c_j^2+s_j^2)]c_j+\sum_{l=1}^{N}\xi_{jl}c_l\right\}+f_j^c$$
$$\frac{d}{dt}s_j=\left\{[-1-p-(c_j^2+s_j^2)]s_j+\sum_{l=1}^{N}\xi_{jl}s_l\right\}+f_j^s. \quad \text{(S-6)}$$

Here c_j and s_j are the normalised amplitudes of two quadrature components of the j-th OPO which corresponds to c and s in Eq. S-3, ξ_{jl} is the coupling coefficient between the j-th and l-th OPOs.

Performance of the proposed network of degenerate OPOs as an Ising machine is tested against the NP-hard MAX-CUT problems on cubic graphs for $N = 4$ to $N = 20$ and on random graphs for $N = 800$ to $N = 20000$. For a graph with N vertices, the $2N$ C-LGEs are solved by the Dormand-Prince method as the differential equation solver [35], in which adaptive integration strength is introduced by evaluating the local truncation error.

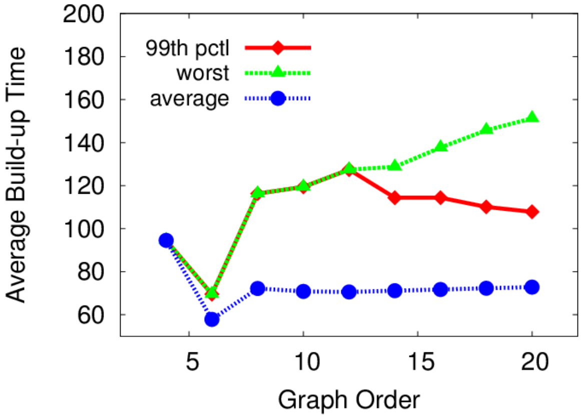

Order	4	6	8	10	12	14	16	18	20
Cubic Graphs	1	2	5	19	85	509	4060	41301	510489

Figure S1: **Numerical results of the build-up time of the OPO networks.** $p = 1.1$ and $\xi = -0.1$. The table indicates the number of cubic graphs for different orders.

Figure S1 shows the normalised build-up time $t = \frac{\gamma_s}{2}\tau$ when the OPO network reaches the steady state oscillation conditions after an above-threshold pump rate ($p = 1.1$) is turned on versus the graph order N. We have numerically tested all graphs, for instance a total number of 510489 graphs are studied for N=20. Most of the build-up time (up to 99% of all graphs) is independent of the graph order N and is on the order of $t \simeq 100$, as shown in Fig. S1. Only slight increase is observed for the worst case as shown in green triangles. Therefore, an actual computational time is determined mainly by the success probability for obtaining a ground state. Since the proposed OPO network is a stochastic machine driven by quantum noise, the success probability is always smaller than one.

Table S1 summarises the performance of the OPO network in solving MAX-CUT problems on cubic graphs. Here, q_{min} denotes the worst-case success probabilities at a fixed pump rate $p = 1.1$ and coupling coefficient $\xi = -0.1$, p_{opt} denotes the optimal pump rate for each worst-case instance, at which the optimum success probability q_{opt} is achieved under the same coupling coefficient $\xi = -0.1$. The success probability at the optimum pump rate for the worst instance is independent of the graph order and ranges from $0.7 \sim 1.0$.

The performance of the OPO network in solving the MAX-CUT problems has also been examined on 71 benchmark instances of the so-called G-set graphs when $p = 1.1$ and $\xi = -0.1$. These instances are randomly constructed by a machine-independent graph generator written by G. Rinaldi, with the number of

Table S1: **Summary of the OPO network in solving the MAX-CUT problems on cubic graphs.**

	Order							
	4	6	8	10	12	14	16	20
q_{min}	0.93	1.00	0.41	0.54	0.52	0.37	0.33	0.11
p_{opt}	1.05	1.30	1.30	1.30	1.00	0.85	0.85	0.82
q_{opt}	1.00	1.00	0.70	0.74	1.00	1.00	1.00	0.74

Table S2: **Performance of the OPO network in solving the MAX-CUT problems on sample G-set graphs.** V is the number of vertices in the graph, E is the number of edges, U_{SDP} is the optimal solution to the semidefinite relaxation of the MAX-CUT problem, and T is the average computation time of the OPO network normalised to the cavity photon lifetime. To make comparisons with the Goemans-Williamson algorithm, every cut value O generated from the network is normalised according to $(O+E_{neg})/(U_{SDP}+E_{neg})$, where $E_{neg} \geq 0$ is the number of negative edges. O_{max} and O_{avg} are the best and the average values in 100 runs, respectively.

Graph	V	E	U_{SDP}	O_{max}	O_{avg}	T
G1	800	19176	12083	0.9591	0.9516	498.82
G6	800	19176	2656	0.9559	0.9506	471.06
G11	800	1600	629	0.9384	0.9254	406.24
G14	800	4694	3191	0.9367	0.9274	498.26
G18	800	4694	1166	0.9308	0.9223	430.24
G22	2000	19990	14136	0.9349	0.9277	768.34
G27	2000	19990	4141	0.9321	0.9270	780.18
G32	2000	4000	1567	0.9328	0.9260	467.42
G35	2000	11778	8014	0.9264	0.9202	602.34
G39	2000	11778	2877	0.9214	0.9152	539.9
G43	1000	9990	7032	0.9373	0.9309	542.92
G48	3000	6000	6000	0.9463	0.9292	762.34
G51	1000	5909	4006	0.9333	0.9242	491.68
G55	5000	12498	11039	0.9070	0.9009	903.46
G57	5000	10000	3885	0.9305	0.9259	648.72
G59	5000	29570	7312	0.9114	0.9074	583.54
G60	7000	17148	15222	0.9037	0.8995	918.98
G62	7000	14000	5431	0.9295	0.9256	719.74
G64	7000	41459	10466	0.9129	0.9092	666.16
G65	8000	16000	6206	0.9284	0.9252	757.28
G66	9000	18000	7077	0.9285	0.9251	786.9
G67	10000	20000	7744	0.9285	0.9260	732.14
G70	10000	9999	9863	0.9433	0.9379	687.28
G72	10000	20000	7809	0.9284	0.9256	748.3
G77	14000	28000	11046	0.9281	0.9256	842.24
G81	20000	40000	15656	0.9268	0.9250	980.54

vertices ranging from 800 to 20000, edge density from 0.02% to 6%, and geometry from random, almost planar to toroidal. The outcomes of running the OPO network 100 times for sample G-set graphs are summarised in Table. S2. Both the best and average outputs of the OPO network are about 2 - 6% better than the 0.878-performance guarantee of the celebrated Goemans-Williamson algorithm based on semidefinite programming (SDP) [36]. Since the differences between the best and the average values are within 1% for most of the instances, reasonable performance is expected for the OPO network even in a single run, which makes the OPO network favourable for applications when response time is the utmost priority. In addition, there is further room to improve the performance, for example by applying local improvement to the raw outcomes of the OPO network and operating the OPO network under optimum pump rate of p and coupling strength of ξ.

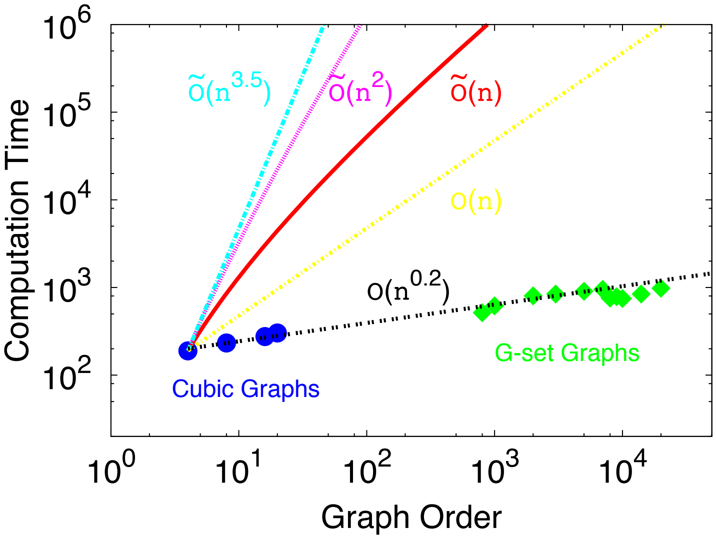

Figure S2: **Average computational time of the OPO network in solving MAX-CUT problems on the worst-case cubic and G-set graphs.** $p = 1.1$ **and** $\xi = -0.1$**.**

The average computational time of the OPO network in solving the MAX-CUT problem on the worst-case cubic and G-set graphs is displayed in Fig. S2. The growth of the computation time fits well to a sub-linear function $O(N^{0.2})$. Computational complexities of best-known algorithms for solving the SDP in the Goemans-Williamson algorithm are also plotted. If a graph with N vertices and m nodes is regular, the SDP can be approximately solved in almost linear time as $\tilde{O}(m) = O(m \log^2(N)\varepsilon^{-4})$ using the matrix multiplicative weights method [37], where ε represents the accuracy of the obtained solution. This behaviour is shown by the red solid line in Fig. S2. However, slower algorithms are required for general graphs. If the edge weights of the graph are all non-negative, the fastest algorithm runs in $\tilde{O}(Nm) = O(Nm \log^2(N)\varepsilon^{-3})$ time based on a Lagrangian relaxation-based method [38]. This computational time is plotted by the pink solid line. For graphs with both positive and negative edge weights, the SDP is commonly solved using the interior-point method which scales as $\tilde{O}(N^{3.5}) = O(N^{3.5} \log(1/\varepsilon))$ [39]. This general computational time for SDP is shown by the blue dashed line. Since the OPO network is applicable to all types of graphs, the sub-linear scaling of the computation time gives it a huge advantage over the SDP algorithm in solving large-scale instances. For instance, the OPO network outputs a solution for the graph G81 with 20000 vertices and 40000 edges in a normalised time of $t \simeq 980$, which corresponds to the actual time of $\tau = 2\gamma_s^{-1}t \simeq 1 \times 10^{-2}$ sec, since the photon lifetime in the large-scale fibre-based OPO network , which can handle this size of problem, is $\sim 6 \times 10^{-6}$ sec (see the last section in this Supplementary Information). This computational time is compared to the time required to run the SDP (interior-point method) using a 1.7 GHz core i7 machine of about $\sim 1 \times 10^5$ sec, which is seven orders of magnitude larger than $\sim 1 \times 10^{-2}$ sec for the OPO network.

3 Details of Experimental Setup

The OPO design shares similarities with the experiment reported in [40]. The ring resonator of the OPO illustrated in Fig. 1b, has a round trip time of 16 ns (a perimeter of ~4.8 m). The setup has two more flat mirrors than the schematic (corresponding to a folded bow tie configuration). All the flat mirrors, except M_1 are gold coated with enhancement dielectric coatings at 2 μm. One of the flat gold mirrors is placed on a translation stage with piezoelectric actuator (PZT). The dielectric mirror (M_1) has a coating which is antireflective at the pump wavelength with less than 0.2% reflection, and is highly reflective (~99%) from 1.8 μm to 2.4 μm. The curved mirrors (M_3 and M_4) have 50-mm radius of curvature and are unprotected gold coated mirrors. The angle of incidence on these mirrors is 4°, which is chosen to compensate the astigmatism introduced by the Brewster-cut nonlinear crystal, and results in ~1 mm of cavity stability range for the spacing between the curved mirrors. The signal beam has a waist radius of 8.3 μm ($1/e^2$ intensity) at the centre of the crystal.

The 1-mm long, Brewster-cut, MgO doped periodically poled lithium niobate (PPLN) crystal has a poling period of 31.254 μm, which is designed to provide degenerate parametric gain for a pump at 1035 nm with type 0 phase matching (e→e+e) at 373 K temperature. The crystal operates at room temperature in the OPO, and even though the phase matching condition is not optimal for the pump (centred at 1045 nm), degenerate operation is achieved by length tuning of the cavity.

Input and output coupling of the signal are achieved with 2-μm thick nitrocellulose pellicles to avoid dispersion in the cavity and etalon effects. In Fig. 1b, the three pairs of "OC" and "IC" are uncoated pellicles (with $2-6\%$ power reflection), the "OC" for the main output is coated (with ~15% power reflection at 2090 nm). The beam splitter in the interferometer (BS) is the same type of coated pellicle. For stabilising the OPO cavity, another uncoated pellicle is used as an output coupler in the resonator (not shown in the schematic).

The pump is a free-running mode-locked Yb-doped fiber laser (Menlo Systems Orange) producing ~80 fs pulses centred at 1045 nm with a repetition rate of 250 MHz, and maximum average power of > 1 W. The filter is a long pass filter at 1850 nm on a Ge substrate to eliminate the pump and transmit the signal.

Gradual pumping is achieved by the chopper, as it causes a rise time (10-90% power) of 180 μs for introducing the pump. The cavity photon lifetime for the signal is estimated to be 60 ns, and the network is pumped ~2.2 times above threshold.

3.1 Servo Loops

Five feedback servo controllers are used to stabilise the length of the cavity, the phase of the delay lines, and the arm-length difference of the interferometer. All the controllers are based on "dither-and-lock" scheme, where a slight modulation (less than 10 nm amplitude at a frequency between 5 and 20 kHz) is applied to a fast PZT, and the error signal is generated electronically by mixing the detector output and the modulated signal [17]. Identical electronic circuits are used with a controller 3-dB bandwidth of 10 Hz.

For the delay lines, the interference of the pump at the other port of the input couplers are used as the input of the controller, and the controller locks the length to achieve destructive interference on the detector, which results in constructive interference on the other port that enters the cavity. The arm length difference of the interferometer is also locked similarly. No phase stabilisation is required for the path from the OPO to the interferometer since all the OPO pulses experience the same path and phase change.

3.2 Free-Running Pump

Here we show that the servo controllers used in the experiment suffice for implementation of the Ising machine and no stabilisation on the pump is required. Slow changes (within the response time of the controller) in the carrier-envelop offset frequency (f_{CEO}^p) and repetition rate (f_R) of the pump do not affect the operation of the Ising machine. Smooth changes in f_R of the pump is intrinsically transferred to the signal since signal pulses are generated from pump pulses. However, the effects of changes in f_{CEO}^p on the Ising machine require taking into account the intrinsic phase locking of the degenerate OPO as well as the role of servo controllers.

The primary task of the servo controller of the OPO is to maximise the output power by matching the roundtrip phase in the resonator to the pulse to pulse phase slip of the pump ($\Delta\phi_p$). The pulse to pulse phase slip is related to f_{CEO}^p by:

$$f_{CEO}^p = \frac{\Delta\phi_p}{2\pi} f_R. \tag{S-7}$$

Assuming the carrier fields for the pump and the signal pulses are defined as: $exp(j\omega_p t + \phi_p)$, and $exp(j\omega_s t + \phi_s)$, respectively, the phase-sensitive gain dictates [17]:

$$\phi_p = 2\phi_s + \pi/2. \tag{S-8}$$

Therefore, if the carrier phase of the pump changes by $\Delta\phi_p$ from one pulse to next, for a single OPO ($T_{cavity} = T_R$), the pulse to pulse phase slip of the signal follows that by:

$$\Delta\phi_s = \Delta\phi_p/2. \tag{S-9}$$

This means that the phase slip of the signal pulses is locked to the phase slip of the pump with a factor of half, which consequently means the f_{CEO} of the pump and signal are locked [17]; the servo loop provides feedback to the cavity to follow this phase slip and maximise the output power. A similar behaviour also happens for a doubly-resonant OPO operating away from degeneracy, with a different ratio between the f_{CEO}s of the pump and signal [41].

For N OPOs in the cavity (i.e. $T_{cavity} = NT_R$), when all OPOs are in the same phase state, the pulse to pulse phase slip in the pump transfers to the OPO to OPO phase slip by a factor of half. Changing phase state from one OPO to another simply means adding π to the phase slip. When a delay line is locked to the top of the interference fringe of the pump pulses, the phase change provided by the delay line at the pump wavelength compensates the pulse to pulse phase slip of pump, i.e. $\phi_D(\omega_p) = \Delta\phi_p$. At the signal wavelength, because $\omega_s = \omega_p/2$ this phase change in the delay line is half ($\phi_D(\omega_s) = \phi_D(\omega_p)/2$), which means that the servo controller compensates the OPO to OPO phase slip resulting from the f_{CEO}^p.

Locking a delay line to top of the fringe of pump pulses corresponds to having either 0 or π phase change for the signal. This is also true for the interferometer. In the experiments, for all the servo controllers, we were able to precisely tune the length from one fringe to the next. This gave us the ability to try different configurations and find the desired coupling phases.

4 OPO Characterisation

When no out coupler is used in the cavity, the OPO has a threshold of 6 mW of pump average power. With all the output and input couplers in the cavity, the threshold reaches 135 mW. Oscillation at degeneracy and away from degeneracy can be achieved depending on the cavity length. The OPO is pumped with 290 mW and the main output of the OPO has 15 mW of average power at degeneracy centred at 2090 nm with the spectrum shown in Fig. S3a. The interferometric autocorrelation of the signal pulses is shown in Fig. S3b suggesting a pulse length of ∼85 fs. The spatial profile of the output beam is very close to Gaussian as shown in Fig. S3c with a radius of ∼1 mm (at $1/e^2$ intensity). The average power of the signal in the delay lines are ∼2 mW, and the intracavity power is estimated to be ∼100 mW.

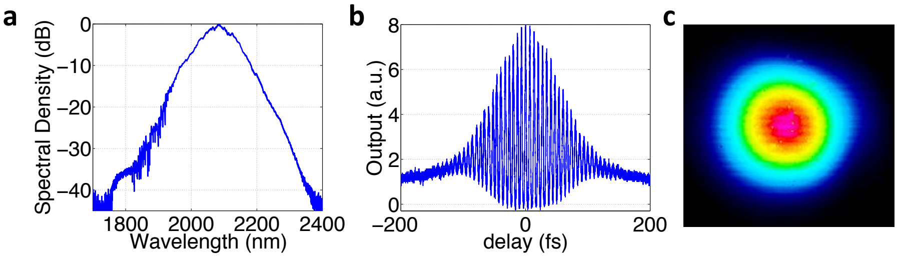

Figure S3: **Summary of the 4-OPO system operation.** **a**, The output spectrum centred at 2090 nm with a 3-db bandwidth of 91 nm. **b**, The interferometric autocorrelation trace of the output pulses with a FWHM of ∼120 fs suggesting Gaussian pulses of ∼85 fs. **c**, The spatial beam profile of the OPO output at 2090 nm.

5 Extended Slow-Detector Results

In Fig. S4 we show the results obtained using a slow detector for different combinations of couplings. Fig. S4 a-c are obtained by scanning the phase of one delay line while the other delay lines are blocked. Delay 1 and 3 have similar effects, because they couple adjacent OPOs but in different directions (Fig. 2b). As shown in Fig. S4 a and c, in-phase coupling by these delays results in the same phase state for all OPOs, and consequently high-intensity interferometer output (I_m); and out-of-phase coupling results in alternating phase states and consequently low-intensity interferometer output (0).

In Fig. S4b we show the interferometer output while the phase of delay 2 is scanned. When the coupling is in-phase, OPO 1 and 3 have the same phase state, and OPO 2 and 4 oscillate in the same phase state. However, these two pairs can either be the same or different, and therefore the output would be either I_m or 0, as shown in Fig. S4b around phase of zero. On the other hand, out-of-phase coupling of delay 2 results in constant output $I_m/2$ as shown in the same plot. Regenerative behaviour of the OPO and its insensitivity to a wide range of phase change in the couplings are observed in these three plots.

When the network is configured to the MAX-CUT problem, we scanned the phase of the delays one by one, and the results are shown in Fig. S4d-f. Different delay phase configurations and the expected outcomes are shown in Table S3, where the last row corresponds to the MAX-CUT problem with all anti-ferromagnetic couplings, and for each of the other rows one of the delay phases is different. For each plot in Fig. S4d-f, the centre of the plot, where the phase of the scanned delay is π, corresponds to the anti-ferromagnetic MAX-CUT problem. The outputs follow the expected outcome.

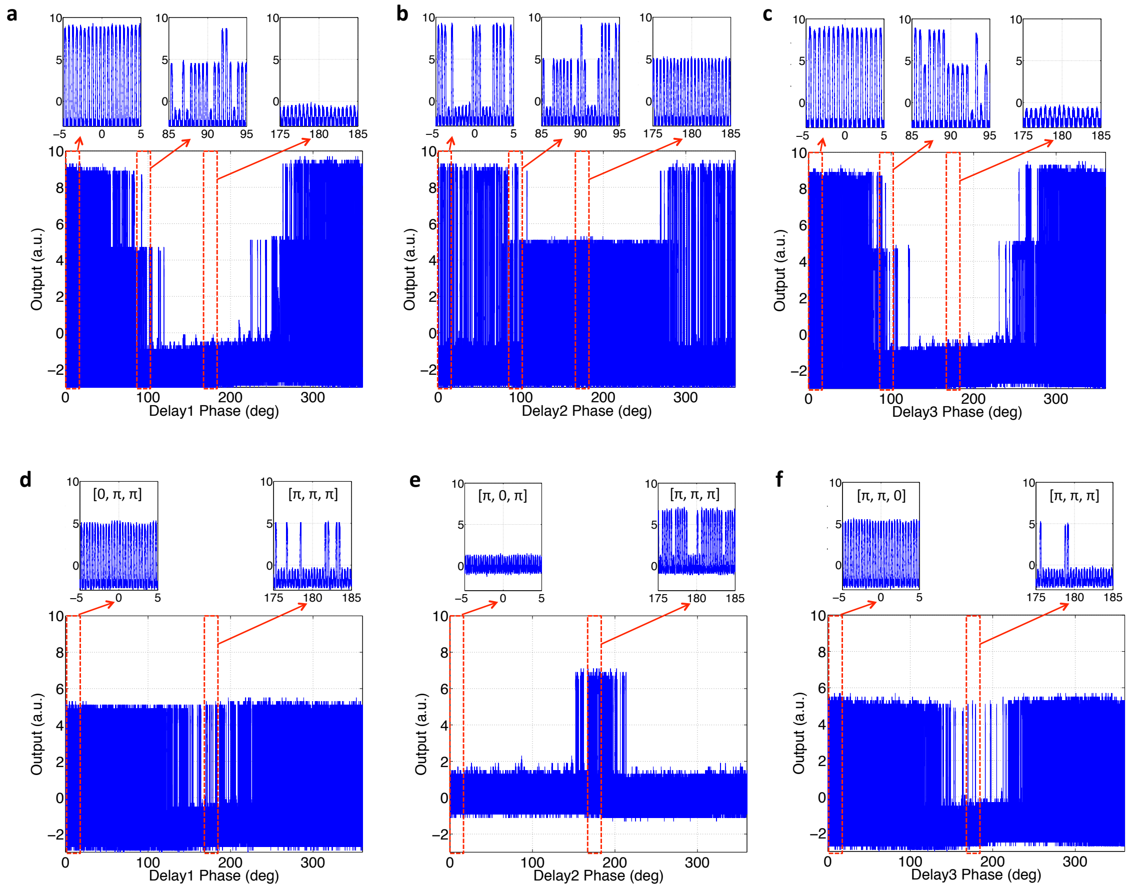

Figure S4: **The output of the slow detector while the phase of one delay is scanned slowly with respect to the chopper, and the other delays are either blocked (a, b, c) or locked to π (d, e, f). a**, Delays 2 and 3 are blocked and phase of delay 1 is scanned. **b**, Delay 1 and 3 are blocked and delay 2 is scanned. **c**, Delays 1 and 2 are blocked and delay 3 is scanned. **d**, Phases of delays 2 and 3 are locked to π and delay 1 is scanned; phase configuration of the network corresponds to $[0, \pi, \pi]$ at 0° and $[\pi, \pi, \pi]$ at 180°. **e**, Phases of delays 1 and 3 are locked to π and delay 2 is scanned; phase configuration of the network corresponds to $[\pi, 0, \pi]$ at 0° and $[\pi, \pi, \pi]$ at 180°. **f**, Phases of delays 2 and 3 are locked to π and delay 1 is scanned; phase configuration of the network corresponds to $[\pi, \pi, 0]$ at 0° and $[\pi, \pi, \pi]$ at 180°.

Table S3: Four configurations for the phases of the delays, the expected phase states of the 4-OPO system, and the expected outcome of the measurements; The last row is the phase configuration corresponding to the MAX-CUT problem, and in the rest of phase configurations one of the delays has a different phase.

Phase of Couplings [D1, D2, D3]	**Expected Phase States**	**Slow Detector**
$[\pi, 0, \pi]$	$\lvert 0\pi0\pi\rangle, \lvert \pi0\pi0\rangle$	100% in 0
$[0, \pi, \pi]$	$\lvert 00\pi\pi\rangle, \lvert \pi00\pi\rangle$, $\lvert 0\pi\pi0\rangle, \lvert \pi\pi00\rangle$	100% in $I_m/2$
$[\pi, \pi, 0]$	$\lvert 00\pi\pi\rangle, \lvert \pi00\pi\rangle$, $\lvert 0\pi\pi0\rangle, \lvert \pi\pi00\rangle$	100% in $I_m/2$
$[\pi, \pi, \pi]$	$\lvert 00\pi\pi\rangle, \lvert \pi00\pi\rangle, \lvert 0\pi\pi0\rangle, \lvert \pi\pi00\rangle$, $\lvert 0\pi0\pi\rangle, \lvert \pi0\pi0\rangle$	66.7% in $I_m/2$, 33.3% in 0

6 Practical Example of a Large-Scale Network

A network of N OPOs can be realised in a single ring resonator with a round-trip time of $T_{cavity} = NT_R$ (T_R is the pulse-to-pulse interval), and constructing $N-1$ delay lines. Schematic of fibre-based implementation of such a machine is illustrated in Fig. S5. To avoid effects of nonlinearities and dispersion in optical fibres, picosecond pump pulses can be used in a long resonator and long delay lines comprising optical fibre components. As an example, for a pump with 10-GHz repetition frequency ($T_R = 100$ ps), a resonator with 200 m of optical fibre results in 10000 temporally separated OPOs. An expected photon lifetime of such a fibre-based OPO network is about $\gamma_s^{-1} \simeq 6 \times 10^{-6}$s, which promises a reasonably fast computational time for a MAX-CUT problem with $N = 10000$.

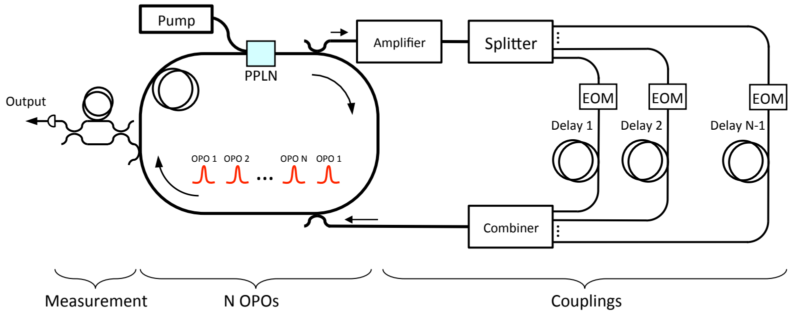

Figure S5: **Schematic of a fibre-based large-scale OPO network.**

The main challenge is stabilising the phases of all these fibre links. Development of extremely low-noise phase-stabilised long (∼100-km) optical fibres [42] promises overcoming this challenge using the existing technologies. Moreover, the regenerative behaviour of the degenerate OPO (as shown in Fig. 3b) suggests that the OPO-based Ising machine can tolerate relatively large phase noise in the couplings.

Similar to the 4-OPO network, each delay line provides a delay of equal to an integer multiple of the repetition period (mT_R), and is responsible for multiple of the Ising coupling terms in the form of $J_{(i)(i+m)}$.

In one delay line, each of these couplings happens at one time slot, and one can use electrooptic phase and amplitude modulators (EOM) to synchronously switch the delay on and off depending on whether the corresponding coupling term is zero or not. This can be extended to synchronously controlling the phases and strengths of the couplings through the delay lines, and hence programming any arbitrary Ising problem on the machine.

References

[31] De Valcarcel, G. J., Patera, G., Treps, N. & Fabre, C. Multimode squeezing of frequency combs. *Phys. Rev. A* **74**, 061801 (R) (2006).

[32] Drumond, P. D., McNeil, K. J. & Walls, D. F. Non-equilibrium transitions in sub/second harmonic generation. II. Quantum theory. *Opt. Acta* **28**, 211–225 (1981).

[33] Risken, H. *The Fokker-Planck Equation: Methods of Solution and Applications.* 2nd ed., Springer-Verlag, Berlin, Germany, 1989.

[34] Haus, H. A. & Yamamoto, Y. Quantum noise of an injection-locked laser oscillator. *Phys. Rev. A* **29**, 1261 (1984).

[35] Dormand, J. R. & Prince, P. J. A family of embedded Runge-Kutta formulae. *J. Comp. Appl. Math.* **6**, 19–26 (1980).

[36] Goemans, M. X. & Williamson, D. P. Improved approximation algorithms for max-cut and satisfiability problems using semidefinite programming. *J. of the ACM* **42**, 1115–1145 (1995).

[37] Arora, S. & Kale, S. A combinatorial, primal-dual approach to semidefinite programs. in *Proceedings of the thirty-ninth annual ACM symposium on Theory of computing*, 227–236 (2007).

[38] Klein, P. & Lu, H. I. Efficient approximation algorithms for semidefinite programs arising from max cut and coloring. in *Proceedings of the twenty-eighth annual ACM symposium on Theory of computing*, 338–347 (1996).

[39] Alizadeh, F. Interior point methods in semidefinite programming with applications to combinatorial optimization. *SIAM J. Optimiz.* **5**, 13–51 (1995).

[40] Rudy, C. W. *et al.* Sub-50 fs pulses around 2070 nm from a synchronously-pumped, degenerate OPO. *Opt. Express* **20**, 27589–27595 (2012).

[41] Lee, K. F. *et al.* Carrier envelope offset frequency of a doubly resonant, nondegenerate, mid-infrared GaAs optical parametric oscillator. *Opt. Lett.* **38**, 1191–1193 (2013).

[42] Grosche, G. *et al.* Optical frequency transfer via 146 km fiber link with 10^{-19} relative accuracy. *Opt. Lett.* **34**, 2270-2272 (2009).